Low-Order Aerodynamic Model for Gust Alleviation Through Wing Morphing

Sebastian Mares*, Arun Vishnu Suresh Babu†
University of North Carolina at Charlotte, Charlotte, NC, 28223

Gust encounters are a critical challenge in modern engineering applications, including urban air mobility (UAM), vertical take-off and landing aircraft (VTOLs), micro-air vehicles (MAVs), and energy harvesting. In these applications, lifting surfaces frequently interact with complex vortical gusts (VGs), resulting in fluctuating loads that deteriorate performance and accelerate fatigue. Inspired by nature, where certain animals leverage external disturbances to reduce energy expenditure, dynamic morphing has been proposed to mitigate these effects and improve performance. This paper presents a novel low-order approach for modeling morphing airfoils under unsteady inflow conditions to ultimately aid in the development of active gust alleviation strategies. Using unsteady thin airfoil theory, we develop an aerodynamic model to predict loads on sections with dynamic trailing-edge flaps (TEFs) interacting with VGs. The airfoil is modeled via a bound-vortex distribution with time-varying flap camber, while the VGs and shed leading- and trailing-edge vortices are represented by discrete vortices. The framework is validated against prior experimental data for rigid airfoils in the presence of external disturbances and morphing airfoils in uniform flow. Parametric studies then quantify the relationship between gust characteristics, airfoil kinematics, aerodynamic loads, and vortex shedding. Results demonstrate that while static flap deflections successfully shift mean lift, they severely amplify cyclic drag and pitching moments. Conversely, dynamic sinusoidal deflections dominate the loading, providing sufficient aerodynamic impact to overpower baseline VG-induced fluctuations. Notably, high-amplitude and high-frequency flapping in the presence of vortical gusts degrades mean lift but enables progressive net thrust generation. Furthermore, altering the rate of flap deflection induces significant phase shifts in the unsteady aerodynamic coefficients relative to local vortex positions, demonstrating that strategic active-TEF kinematics have the potential to effectively mitigate adverse gust effects.

I. Nomenclature

$A_n(t)$	time-dependent Fourier coefficients of bound-vorticity, dimensionless
C_D, C_L, C_M, C_N, C_S	drag, lift, pitching-moment, normal-force, and suction-force coefficients, dimensionless
$c, c_{\text{eff}}(t)$	reference chord and effective chord length, dimensionless
c_a, c_f, c_{pvt}	main-element length, flap-element length, and pivot distance from LE, dimensionless
$h(t)$	plunge displacement (positive upward), dimensionless
U, U_{ref}	freestream speed and reference speed, dimensionless
$u_{\text{ind}}, w_{\text{ind}}$	vortex induced velocities in the inertial frame, dimensionless
$W(\xi, t), W(\nu, t)$	downwash in the morphing and non-morphing body fixed frames, dimensionless
$\alpha(t), \alpha_\delta(t), \alpha_{\text{eff}}(t)$	pitch angle, flap-induced increment, and effective angle of attack, rad
$\Gamma_B, \Gamma_{\text{LEV}}, \Gamma_{\text{TEV}}$	bound, leading-edge shed, and trailing-edge shed circulations, dimensionless
γ	bound-vorticity distribution, dimensionless
$\delta(t)$	flap deflection (positive downward), rad
η, ξ	body-fixed chord-normal and chord-wise coordinates, dimensionless
θ, ν	variables of the Glauert transformation, rad
ρ	fluid density

*Undergraduate Research Assistant, Mechanical Engineering and Engineering Science, smares2@charlotte.edu, AIAA Student Member 1799160
†Teaching Assistant Professor, Mechanical Engineering and Engineering Science, asures10@charlotte.edu

II. Introduction

Unsteady aerodynamic flows are of relevance in many modern engineering applications, including flapping-wing micro air vehicles (MAVs), urban air mobility (UAM), formation flight, wind energy harvesters, vertical take-off and landing aircraft (VTOLs), bio-inspired flyers, and airfoils. While schools of fish and flocks of birds exploit oncoming vortices to reduce energetic cost, engineered rotors often suffer when external disturbances such as vortical gusts amplify unsteady loads and accelerate fatigue. In wind turbine arrays, downstream blades are repeatedly subjected to upstream turbine wakes, tower-generated vortex streets leading to unsteady flow induced loads that degrade performance [1]. Dynamic morphing has been suggested as an approach to mitigate these effects and improve performance. Active trailing-edge flaps (TEFs) have been explored in the context of wind turbines to achieve load modulation through active camber variation [2], making them highly attractive for applications where periodic body-gust encounters present challenges.

These disturbance encounters, such as vortical gusts in urban environments, are characterized by complex flow field interactions that frequently induce flow separation and alter the timing and intensity of leading-edge vortex (LEV) formation, dynamic stall onset, and force transients. An airfoil subjected to these external gusts exhibits large unsteady forces and LEV dynamics that depend sensitively on the structure and frequency of the incoming vortices, as well as the vertical offset of the section relative to the centerline of the disturbance [3]. Ultimately, these externally generated disturbances alter the lift history of an airfoil through phase-dependent interruption or reinforcement of LEV shedding [4]. Because these resulting unsteady load fluctuations lead to significant stability, control, and fatigue issues, a variety of flow control strategies have been explored to modulate these loads and delay the onset of dynamic stall. Recent research efforts have demonstrated that careful motion design and kinematics can successfully regulate LEV characteristics and mitigate gust effects [5].

While high-fidelity CFD resolves these complex separation mechanisms and unsteady flow phenomena, it remains computationally prohibitive for extensive parametric design sweeps. Physics-based low-order models strike a necessary balance between fidelity and cost. By isolating the dominant aerodynamic mechanisms from the computational overhead of full Navier-Stokes simulations, these models become highly advantageous for rapidly evaluating thousands of kinematic and gust parameter combinations. This rapid iteration is essential for preliminary design and the development of active control strategies. For example, the LESP-modulated discrete-vortex method (LDVM) [6].

In this work, we present a novel low-order model for morphing airfoils subject to vortical disturbances. We apply unsteady thin airfoil theory to predict the resulting loads on airfoil sections with dynamic TEFs in the presence of vortical gusts (VGs). Large, rapid TEF deflections challenge classical assumptions; therefore, we utilize a morphing-airfoil formulation that treats the effective chord line as time-varying to improve load predictions under substantial camber changes, as presented by Martínez-Carmena and Ramesh [7]. We embed TEFs within this framework and introduce externally generated, vortex-street-like disturbances representative of gust interactions. The model is validated against prior experimental data for rigid airfoils in the presence of external disturbances and literature data for morphing airfoils in uniform flow. We then characterize how flap kinematic parameters, specifically static deflection angle, oscillation amplitude, and actuation frequency affect the transient force histories and vortex shedding patterns, evaluating how active TEF strategies can counteract destructive load excursions and enhance aerodynamic performance.

III. Theoretical Background

The theoretical framework used in this work extends the discrete-vortex method of SureshBabu et al. [4] by incorporating the morphing-airfoil formulation of Martínez-Carmena and Ramesh [7]. Whereas the latter did not consider leading-edge vorticity, the present study explicitly includes the shedding of leading-edge vortices (LEVs) in the aerodynamic results for airfoils subjected to vortical gusts. The following subsections detail this theory.

A. Low-order model for a non-morphing airfoil in the presence of VGs

Figure 1 depicts an airfoil at time t translating leftward at speed U with arbitrary pitch and heave. These kinematics are defined in the inertial frame OXZ, where the airfoil pitches about a pivot x_p. A body-fixed frame Bxz, originating at the leading edge (LE) and aligned with the chord-wise (x) and chord-normal (z) directions, coincides with the inertial frame at $t = 0$. VGs are modeled as upstream-released vortical clusters.

Following thin-airfoil theory, a continuous bound circulation distribution $\gamma(x, t)$ models the airfoil. Using the Glauert transformation $x = \frac{c}{2}(1 - \cos \nu)$ yields:

$$\gamma(\nu,t) = 2U_{\text{ref}}\left[A_0(t)\frac{1+\cos\nu}{\sin\nu} + \sum_{n=1}^{\infty} A_n(t)\sin(n\nu)\right] \tag{1}$$

where U_{ref} is typically set to U. The Fourier coefficients $A_n(t)$ are determined by enforcing the zero-normal-flow boundary condition at all times t. Absent a trailing-edge flap or time-varying camber, this condition yields the following expressions for $A_n(t)$:

$$A_0(t) = -\frac{1}{\pi U_{\text{ref}}}\int_0^{\pi} W(\nu,t)\,d\nu \tag{2a}$$

$$A_n(t) = \frac{2}{\pi U_{\text{ref}}}\int_0^{\pi} W(\nu,t)\cos(n\nu)\,d\nu \tag{2b}$$

The downwash W is the velocity induced along the airfoil in the direction opposite to the normal to the camber line, expressed as:

$$W(x,t) = \frac{\partial\eta}{\partial x}\left(U\cos\alpha + \dot{h}\sin\alpha + u_{\text{ind}}(x)\right) - U\sin\alpha - \dot{\alpha}(x-x_p) + \dot{h}\cos\alpha - w_{\text{ind}}(x) \tag{3}$$

Here, $\partial\eta/\partial x$ is the slope of the camber line. Equation (3) accommodates large pitch angles where traditional small-angle approximations are invalid.

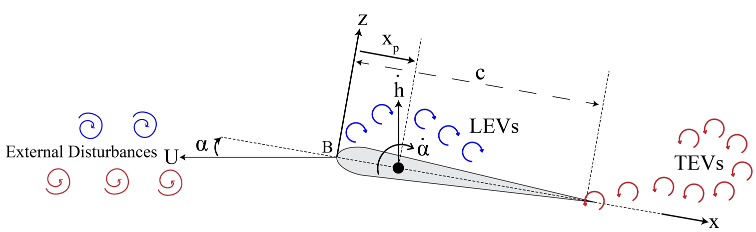

Figure 1. Illustration of the low-order framework (without trailing-edge flap) showing the oncoming flow disturbances, the vorticity shed from the airfoil and the kinematic variables used in the theoretical formulation of the LDVM. Clockwise vorticity is considered positive.

Per Kelvin's circulation theorem, a discrete trailing-edge vortex (TEV) is shed at each time step, positioned one-third of the distance from the trailing edge to the previously shed TEV. Absent LEV shedding, the TEV released at the jth time step has a strength Γ^j_{TEV} such that:

$$\Gamma^j_B + \Gamma^j_{\text{TEV}} = \Gamma^{j-1}_B \tag{4}$$

where $\Gamma_B = \int_0^{\pi}\gamma(\nu)\,d\nu = \pi c U_{\text{ref}}[A_0(t) + 0.5A_1(t)]$. The strength of the latest TEV can be obtained after some manipulation of Eqn. (4) as:

$$\Gamma^j_{\text{TEV}} = \frac{\Gamma^{j-1}_B + c\int_0^{\pi} W^0(1-\cos\nu)\,d\nu}{1 - c\int_0^{\pi} W'_{\text{TEV}}(1-\cos\nu)\,d\nu} \tag{5}$$

Here, W'_{TEV} is the downwash induced by a unit-strength discrete vortex at the latest TEV location, and W^0 is the downwash from all other factors excluding the latest TEV (computed via Eq. (3)).

Discrete LEVs are shed when the leading-edge suction parameter ($\mathcal{L}$, set to A_0 here) exceeds a critical threshold, $\mathcal{L}_{crit}$. During active shedding, the strengths of the LEV and TEV released at each time step must simultaneously satisfy the Kelvin condition and maintain $\mathcal{L} = \mathcal{L}_{crit}$. This yields a two-variable problem of the form:

$$\left[A\right]\begin{Bmatrix}\Gamma_{\text{TEV}}\\ \Gamma_{\text{LEV}}\end{Bmatrix} = \left\{B\right\} \tag{6}$$

where

$$\left[A\right] = \begin{bmatrix} 1 - c\int_0^{\pi} W'_{\mathrm{TEV}}(1-\cos\nu)d\nu & 1 - c\int_0^{\pi} W'_{\mathrm{LEV}}(1-\cos\nu)d\nu \\ \int_0^{\pi} W'_{\mathrm{TEV}} d\nu & \int_0^{\pi} W'_{\mathrm{LEV}} d\nu \end{bmatrix} \tag{7}$$

and

$$\left\{B\right\} = \begin{Bmatrix} \Gamma_B^{j-1} + c\int_0^{\pi} W^0(1-\cos\nu)d\nu \\ -\pi U_{\mathrm{ref}}\mathcal{L}_{crit} - \int_0^{\pi} W^0 d\nu \end{Bmatrix} \tag{8}$$

where W'_{LEV} is the downwash induced by a unit-strength discrete vortex at the latest LEV location. With the discrete vortex strengths determined, the flowfield solution is finalized by computing the Fourier coefficients and the corresponding bound-vortex distribution to satisfy the zero-normal-flow boundary condition.

The normal and suction forces per unit span are expressed in terms of the Fourier coefficients. To facilitate the transition to a morphing framework, the normal force F_N is is expressed as:

$$\begin{aligned} F_N &= \rho\pi c U_{\mathrm{ref}}\left(U\cos\alpha + \dot{h}\sin\alpha\right)\underbrace{\left(A_0 + \frac{1}{2}A_1\right)}_{A_{\mathrm{term},1}} + \rho\pi c^2 U_{\mathrm{ref}}\underbrace{\left(\frac{3}{4}\dot{A}_0 + \frac{1}{4}\dot{A}_1 + \frac{1}{8}\dot{A}_2\right)}_{A_{\mathrm{term},2}} \\ &+ \rho\int_0^c u_{\mathrm{ind}}(x)\gamma(x,t)dx + \rho c\dot{\Gamma}_{\mathrm{LEV}} \end{aligned} \tag{9}$$

The suction force per unit span is $F_S = \rho\pi c U_{\mathrm{ref}}^2 A_0^2$. Nondimensionalizing these by $\frac{1}{2}\rho U_{\mathrm{ref}}^2 c$ yields the coefficients $C_{N,t}$, $C_{N,nc}$, $C_{N,\nu}$, and C_S. The lift and drag coefficients are then:

$$C_L = C_N\cos\alpha + C_S\sin\alpha \tag{10}$$

$$C_D = C_N\sin\alpha - C_S\cos\alpha \tag{11}$$

The aerodynamic moment M about an arbitrary reference point x_{ref} is similarly partitioned:

$$\begin{aligned} M = x_{\mathrm{ref}}F_N - \rho\pi c^2 U\Big[&\left(U\cos\alpha + \dot{h}\sin\alpha\right)\underbrace{\left(\tfrac{1}{4}A_0 + \tfrac{1}{4}A_1 - \tfrac{1}{8}A_2\right)}_{A_{\mathrm{term},3}} + c\underbrace{\left(\tfrac{7}{16}\dot{A}_0 + \tfrac{11}{64}\dot{A}_1 + \tfrac{1}{16}\dot{A}_2 - \tfrac{1}{64}\dot{A}_3\right)}_{A_{\mathrm{term},4}}\Big] \\ &- \rho\int_0^c u_{\mathrm{ind}}(x)\gamma(x,t)x\,dx - \frac{\rho c^2\dot{\Gamma}_{\mathrm{LEV}}}{2} \end{aligned} \tag{12}$$

The nondimensional moment coefficient is $C_M = M/(\frac{1}{2}\rho U_{\mathrm{ref}}^2 c^2)$.

B. Low-order model for a morphing airfoil in the presence of VGs

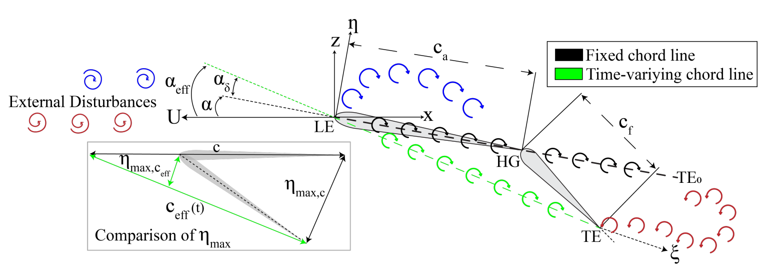

Figure 2. Low order framework with TEF showing external disturbances, shed vorticity, bound vortices representing the fixed chord line, bound vortices representing the time-varying chord line, and the kinematic variables used.

To incorporate morphing, we follow the approach of Martínez-Carmena and Ramesh [7], which utilizes a time-varying "effective chord line" connecting the leading and trailing edges (Fig. 2). The length of this effective chord is expressed as:

$$c_{\text{eff}}(t) = \sqrt{c_a^2 + c_f^2 + 2c_a c_f \cos\delta(t)} \tag{13}$$

A body-fixed reference frame (ξ, η) is attached to the camber line, with its origin at the LE and the ξ-axis aligned with the effective chord line (Fig. 2). Due to flap deflection, the effective chord line forms an effective angle of attack $\alpha_{\text{eff}}(t) = \alpha(t) + \alpha_\delta(t)$, where α_δ accounts for the rotation of the effective chord line:

$$\alpha_\delta(t) = \arcsin\left(\frac{c_f}{c_{\text{eff}}(t)} \sin\delta(t)\right) \tag{14}$$

The chord-wise coordinate ξ and the piece-wise camber distribution $\eta(\xi)$ are defined as:

$$\xi = \frac{c_{\text{eff}}}{2}(1 - \cos\theta) \tag{15}$$

$$\eta(\xi) = \begin{cases} \xi \tan\alpha_\delta & \xi_{\text{LE}} < \xi < \xi_{\text{HG}} \\ (c_{\text{eff}} - \xi)\tan(\delta - \alpha_\delta) & \xi_{\text{HG}} < \xi < \xi_{\text{TE}} \end{cases} \tag{16}$$

where $\xi_{\text{LE}} = 0$, $\xi_{\text{TE}} = c_{\text{eff}}$, and $\xi_{\text{HG}} = c_a \cos\alpha_\delta$ are the coordinates of the leading edge, trailing edge, and hinge, respectively.

In the unsteady flow scenario, the zero-normal flow condition $\mathbf{v} \cdot \mathbf{n} = 0$ is enforced. The fluid velocity $\mathbf{v}$ results from body kinematics, surface deformations, vortical gusts, and free vortices (Fig. 2). The downwash $W(\xi, t)$ for the morphing airfoil is expressed as:

$$\begin{aligned} W(\xi, t) = \frac{\partial\eta}{\partial\xi}\Big(&u_{\text{ind}}(\xi) + U\cos\alpha_{\text{eff}} + \dot{h}\sin\alpha_{\text{eff}} - \dot{\alpha}(\eta - \eta_{\text{pvt}}) - \dot{\alpha}_\delta\eta + \dot{\xi}\Big) \\ &- w_{\text{ind}}(\eta) - U\sin\alpha_{\text{eff}} + \dot{h}\cos\alpha_{\text{eff}} - \dot{\alpha}(\xi - \xi_{\text{pvt}}) - \dot{\alpha}_\delta\xi + \dot{\eta} \end{aligned} \tag{17}$$

where the induced velocities are obtained by transforming the inertial-frame velocities into the body-fixed morphing frame as follows:

$$u_{\text{ind}}(\xi) = u_{\text{ind}}\cos\alpha_{\text{eff}} - w_{\text{ind}}\sin\alpha_{\text{eff}} \tag{18}$$

$$w_{\text{ind}}(\eta) = u_{\text{ind}}\sin\alpha_{\text{eff}} + w_{\text{ind}}\cos\alpha_{\text{eff}} \tag{19}$$

The downwash is then used to determine the Fourier coefficients $A_0(t)$ and $A_n(t)$ as defined in Equation (2), where $W(\nu, t)$ is replaced by $W(\xi, t)$. Integrating the bound vorticity over the time-varying chord line yields the bound circulation:

$$\Gamma_B(t) = \pi c_{\text{eff}} U_{\text{ref}} \left[A_0(t) + 0.5A_1(t)\right] \tag{20}$$

The strengths of the vortices shed from the airfoil are determined in satisfaction of Kelvin's circulation theorem. The aerodynamic loads are partitioned into components that mirror the rigid-body formulations while explicitly accounting for the time-varying chord and effective angle of attack. The total normal force coefficient C_N is:

$$C_N = C_{N,nc} + C_{N,t} + C_{N,r} + C_{N,d} + C_{N,v} + \frac{2\dot{\Gamma}_{\text{LEV}}}{U_{\text{ref}}^2} \tag{21}$$

The translational ($C_{N,t}$), non-circulatory ($C_{N,nc}$), and vortex-induced ($C_{N,v}$) components utilize the forms established in Eqn. (9), but are computed using c_{eff} and α_{eff} as follows:

$$C_{N,t} = \frac{2\pi c_{\text{eff}}}{cU_{\text{ref}}}\left(U\cos\alpha_{\text{eff}} + \dot{h}\sin\alpha_{\text{eff}}\right)A_{\text{term},1} \tag{22a}$$

$$C_{N,nc} = \frac{2\pi c_{\text{eff}}^2}{cU_{\text{ref}}}A_{\text{term},2} \tag{22b}$$

$$C_{N,v} = \frac{2}{U_{\text{ref}}^2 c}\int_0^{c_{\text{eff}}} u_{\text{ind}}(\xi)\gamma(\xi)d\xi \tag{22c}$$

The unique contributions from morphing kinematics, rotation ($C_{N,r}$) and deformation ($C_{N,d}$), are expressed as:

$$C_{N,d} = \frac{2}{U_{\text{ref}}^2 c}\int_0^{c_{\text{eff}}} \dot{\xi}\gamma(\xi)d\xi \tag{23a}$$

$$C_{N,r} = -\frac{2}{U_{\text{ref}}^2 c}\int_0^{c_{\text{eff}}} \left(\dot{\alpha}(\eta - \eta_{\text{pvt}}) + \dot{\alpha}_\delta\eta\right)\gamma(\xi)d\xi \tag{23b}$$

The suction force coefficient is $C_S = 2\pi A_0^2$. The pitching moment coefficient C_M about the pivot point may be expressed as:

$$\begin{aligned} C_M =& \; C_N \frac{c_{\text{pvt}}}{c} \cos\alpha_\delta - \frac{2\pi c_{\text{eff}}^2 U}{U_{\text{ref}}^2 c^2} \left[\left(U\cos\alpha_{\text{eff}} + \dot{h}\sin\alpha_{\text{eff}} \right) A_{\text{term},3} - c A_{\text{term},4} \right] \\ &+ \frac{2}{U_{\text{ref}}^2 c^2} \int_0^{c_{\text{eff}}} \left(\dot{\alpha}(\eta - \eta_{\text{pvt}}) + \dot{\alpha}_\delta \eta - \dot{\xi} - u_{\text{ind}}(\xi) \right) \gamma(\xi) \xi d\xi - \frac{\dot{\Gamma}_{\text{LEV}}}{U_{\text{ref}}^2} \end{aligned} \tag{24}$$

IV. Results

Table 1 summarizes the key parameters for the validation and parametric case studies. The low-order model is first validated against experimental [4, 8] and numerical benchmarks [7]. Subsequently, parametric studies demonstrate the framework's capability to simulate complex scenarios by accounting for both vortical gusts and LEV shedding.

Table 1. Summary of case studies and aerodynamic parameters.

Description	α (deg)	$\delta_{\max}$ (deg)	f_{Flap}	VG Status	c_f/c
Validation Cases					
SureshBabu et al. [4]	6	0	—	Active	0.5
Medina et al. [8]	0	20	Ramp	Inactive	0.5
Parametric Studies					
Effect of Statically Deflected Flap	0	±30	Static	Active	0.5
Effect of Sinusoidal Deflection Amplitude	0	5–30	$1.0f_{\text{Shed}}$	Active	0.5
Effect of Flap Deflection Rate	0	30	0.25–$1.0f_{\text{Shed}}$	Active	0.5

A. Static airfoil in the presence of vortical gusts

To validate the model, Fig. 3 compares the predicted lift coefficient of a static airfoil at 6° incidence against measured values from SureshBabu et al. [4]. For a vortical gust (VG) frequency of $f = 0.2$ Hz, panel (a) shows the measure lift, whereas panels (b) and (c) present the model-predicted lift histories for the rigid and morphing frameworks, respectively. By reproducing the experimental conditions, this comparison serves as a direct validation between frameworks.

Unless specified otherwise, all studies are performed with a 50% chord trailing-edge flap and utilize a nondimensional timestep $\delta t^* = 0.015$, a vortex cluster strength $\Gamma/(cU_\infty) = 0.3$, and a uniform-flow speed of $0.882U_\infty$ ($0.964U_\infty$ when disturbances are inactive). Each VG is modeled as a cluster of 50 discrete vortices released $15c$ upstream of the leading edge with a release radius of $0.075c$.

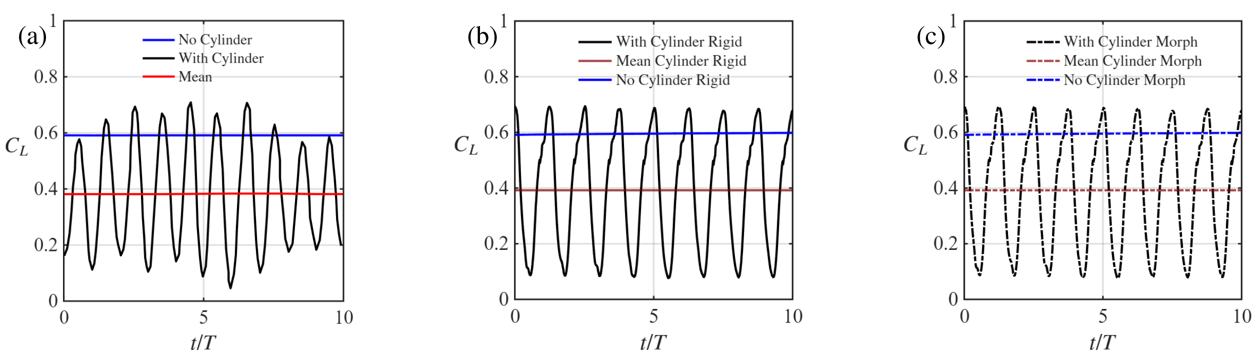

Figure 3. Validation of the model prediction for a static nonmorphing airfoil at 6° incidence in the presence of vortical gusts: (a) experimentally observed C_L [4], (b) C_L predicted by the rigid model, (c) C_L predicted by the morphing model.

The low order model demonstrates excellent qualitative and quantitative agreement with the experimental data [4], faithfully capturing the oscillatory behavior with a cycle period $T = 1.2486$ s. The model predicts a mean lift coefficient of $\bar{C}_L = 0.3844$ in the presence of VGs. This represents a 34.6% reduction from the steady-state value of $\bar{C}_L = 0.5968$ calculated in uniform flow. This reduction aligns with previous reports [4] of mean lift loss for static airfoils positioned near the centerline of a bluff body wake. The model demonstrates that whereas the oscillation amplitude is largely determined by the vortex cluster strength, the mean lift primarily depends on the uniform-flow speed. This performance drop stems from the interaction between the airfoil's bound vorticity and the discrete VG clusters.

As evidenced by Fig. 4, lift oscillations correlate with the spatial features of the oncoming disturbance: a local lift peak occurs with a clockwise (CW) vortex near the upper mid-chord and a counter-clockwise (CCW) vortex near the lower leading edge. Conversely, a lift valley occurs when an approaching CW vortex reaches the upper leading edge.

Furthermore, the consistency between panels (b) and (c) confirms the integrity of the morphing framework at $\delta = 0°$. Both models converge to identical mean values for lift, drag ($\bar{C}_D = -0.0135$), and pitching moment ($\bar{C}_M = -0.0146$). Compared to steady-state uniform flow ($\bar{C}_D = 0.0013$ and $\bar{C}_M = 0.0005$), these represent an increase in mean drag and pitching moment by factors of 10.8 and 20.75, respectively, validating the model for subsequent studies.

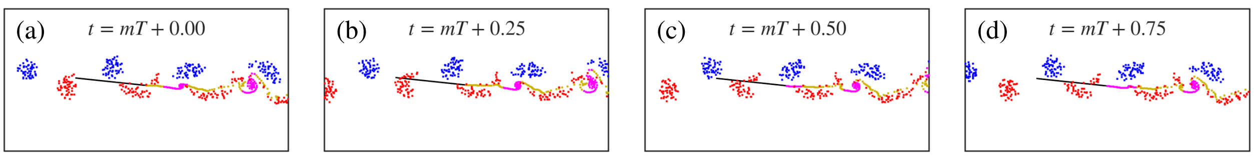

Figure 4. Discrete-vortex predictions at four instants during a lift oscillation cycle from Figure 3: (a) $t = mT$, (b) $t = mT + 0.25$, (c) $t = mT + 0.5$, (d) $t = mT + 0.75$, where T is the cycle period and m is an integer. Vortex colors (positive/negative): LEVs (green/orange), TEVs (yellow/magenta), VGs (blue/red), and airfoil bound vortices (black).

B. Morphing airfoil in uniform freestream

To validate the morphing model, Fig. 5 compares the aerodynamic response of an airfoil featuring a 50% trailing-edge flap against the experimental measurements of Medina et al. [8]. The simulation strictly replicates the experimental conditions, utilizing a free-stream velocity of $U_\infty = 0.2$ m/s and a total chord of $c = 0.2$ m. Under these conditions, the model-predicted lift, drag, and pitching-moment coefficients are presented for a main element at 0° incidence, with the flap undergoing a 20° downward half-sinusoid ramp-and-hold over convective times of 0.5, 1, 2, and 4 tU/c.

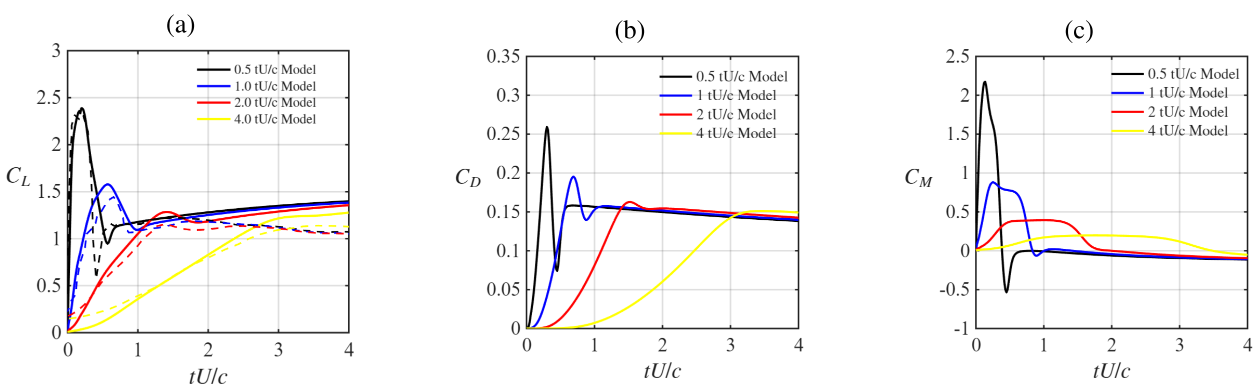

Figure 5. Model validation for a morphing airfoil with the main element at 0° incidence and a trailing-edge flap deflected 20° downward using a half-sinusoid ramp-and-hold over convective times of 0.5, 1, 2, and 4 tU/c in uniform flow: (a) C_L (experiment [8] vs. model), (b) C_D (model), and (c) C_M (model). Dashed lines correspond to experimental data available in [8].

As illustrated in Figure 5, the low-order framework successfully captures the rate-dependent aerodynamic response of the morphing airfoil, demonstrating its capability to accurately resolve the transient loads induced by varying flap deflection rates in uniform flow.

C. Morphing airfoil in the presence of vortical gusts: static flap deflection

Before exploring dynamic kinematics, it is essential to establish how static flap deflections influence the airfoil's interaction with vortical gusts (VGs). In Figure 6, the low-order model evaluates the morphing airfoil (main element at 0° incidence) with the trailing-edge flap statically deflected from $\delta = -30°$ to $+30°$. Subjected to a continuous Kármán vortex street, the airfoil experiences a periodic lift oscillation cycle of $T = 0.9995$ s. This provides a baseline for evaluating how fixed flap angles alter sensitivity to an vortical gusts.

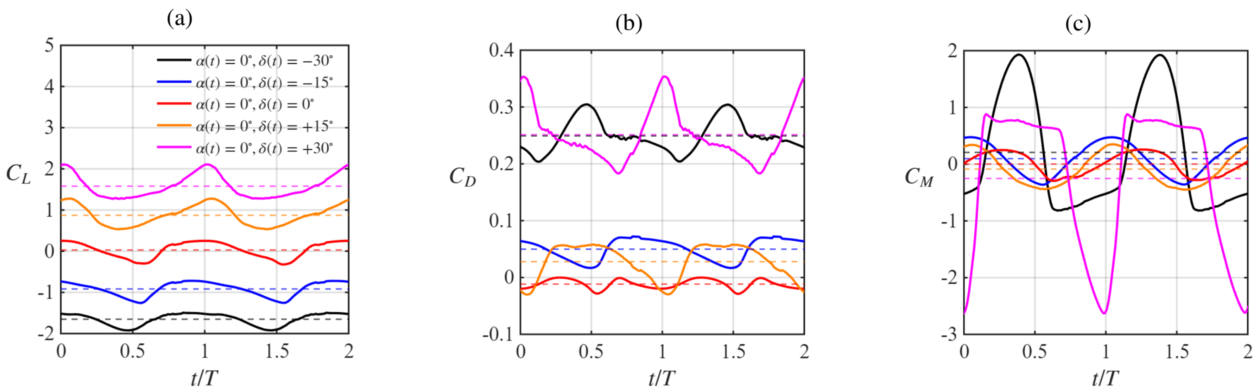

Figure 6. Comparing the effect of a statically deflected trailing-edge flap with main-element at 0° incidence in the presence of vortical gusts: (a) C_L, (b) C_D, and (c) C_M predicted by the morphing low-order model.

Altering the static deflection predictably shifts the mean lift coefficient (Figure 6a). Downward (positive) deflections increase mean lift ($\bar{C}_L = 1.5610$ at $+30°$), whereas upward (negative) deflections produce a symmetric degradation ($\bar{C}_L = -1.6562$ at $-30°$). Despite these these shifts in the mean aerodynamic coefficients, the peak-to-peak lift amplitude remains uniform, indicating that lift oscillations are primarily driven by the passing VGs rather than the static angle.

However, drag and pitching moment histories (Figures 6b and 6c) show larger oscillation amplification at higher deflections. Whereas the baseline $\delta = 0°$ case exhibits minimal drag variations ($\bar{C}_D = -0.0111$), increasing the deflection magnitude raises the mean drag ($\bar{C}_D \approx 0.25$ for $\pm 30°$) and causes nonlinear fluctuations as the flap acts as a flow obstruction. Similarly, the mean moment shifts accordingly, nose-down ($\bar{C}_M = -0.1639$ at $+30°$) and nose-up ($\bar{C}_M = 0.2742$ at $-30°$), but experiences shifts of nearly $\Delta C_M \approx 3$ within a single cycle.

The wake interactions driving these nonlinear load fluctuations for the $+30°$ case are visualized in Figure 7. A local peak in both lift and drag corresponds to a clockwise (CW) vortex at the hinge/mid-chord alongside a counter-clockwise (CCW) vortex at the leading edge. Conversely, local lift and drag valleys align with a CW vortex near the leading edge and a CCW vortex near the mid-chord/hinge. Finally, the pitching moment peaks when a CW vortex is at the mid-chord and a CCW vortex is at the leading edge, and drops to a valley when the CW vortex is at the leading edge and the CCW vortex is near the hinge. Notably, as the CCW vortex approaches the mid-chord and carries away leading-edge vortices (LEVs), the corresponding C_M peak is visibly flattened.

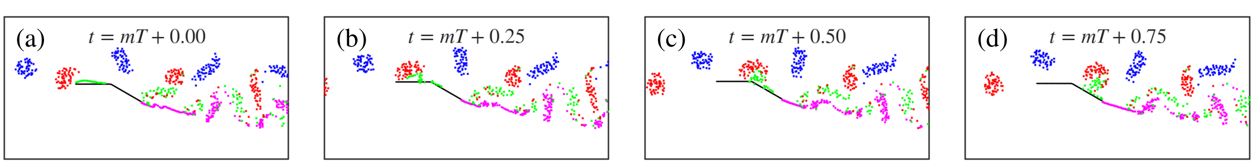

Figure 7. Discrete-vortex plots from the model predictions at four time instants in a cycle of lift oscillation in Figure 6.

This static study demonstrates how static flap deflections successfully alter the mean lift but strongly sensitize drag and pitching moment to the unsteady wake, resulting in severe cyclic loading.

D. Morphing airfoil in the presence of vortical gusts: dynamic flap deflection

In Figure 8, the steady-state periodic response of a morphing airfoil (main element at 0° incidence) subjected to VGs is evaluated for continuous sinusoidal flap deflections ranging from $\delta_{max} = 5°$ to $30°$. Increasing the maximum deflection systematically increases the oscillation amplitudes for C_L, C_D, and C_M. This scaling demonstrates that a large portion of the dynamic loading is dictated by the severity of the flap kinematics, overpowering the baseline variations caused solely by the VGs. Consequently, this indicates that if a trailing-edge flap is deflected strategically in response to vortical gusts, it possesses sufficient impact on the aerodynamic loads to counteract vortex-induced oscillations.

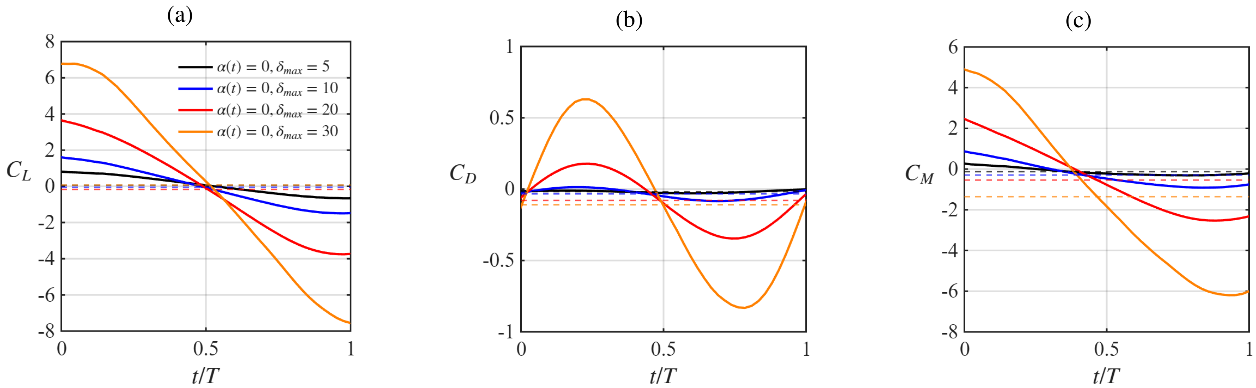

Figure 8. Comparing the effect of a sinusoidally deflecting trailing-edge flap with main-element at 0° incidence in the presence of vortical gusts: (a) C_L, (b) C_D, and (c) C_M predicted by the morphing low-order model.

Furthermore, increasing the flap amplitude fundamentally alters the mean aerodynamic loads. The mean lift coefficient degrades progressively, dropping from $\bar{C}_L = -0.0975$ at 5° to -0.1883 at 10°, -0.3479 at 20°, and -0.4769 at 30°. A corresponding shift occurs in the mean pitching moment, which develops a nose-down bias: $\bar{C}_M = -0.2374$ (5°), -0.4814 (10°), -0.1005 (20°), and -1.5699 (30°).

Conversely, a major aerodynamic benefit is shown when examining the drag coefficient: increasing the amplitude yields progressive thrust generation. The mean drag coefficient shifts further below zero with higher deflections, improving from $\bar{C}_D = -0.0048$ (5°) and -0.0191 (10°) to -0.0741 (20°) and -0.1599 (30°), confirming the flap's ability to enhance the extraction of thrust from the oncoming wake.

The physical mechanisms driving these load trends for the 30° case are visualized in Figure 9 in the form of flow snapshots in a single oscillatory cycle. A local peak in lift is associated with a clockwise (CW) vortex near the mid-chord and a counter-clockwise (CCW) vortex near both the leading and trailing edges on the lower surface, whereas a lift valley occurs when a CW vortex is near the hinge/mid-chord alongside a CCW vortex pair on the lower surface.

In the case of drag, a local peak in drag corresponds to a CW vortex at the hinge/mid-chord and a CCW vortex on the lower leading edge, whereas a drag valley (peak thrust) corresponds to a CW vortex at the leading edge (Fig. 9b) and a CCW vortex at the hinge on the lower surface (Fig. 9d).

Finally, pitching moment peaks correspond to a CW vortex at the hinge and a CCW vortex near the leading edge, whereas moment valleys align with a CW vortex at the leading edge and a CCW vortex at the hinge.

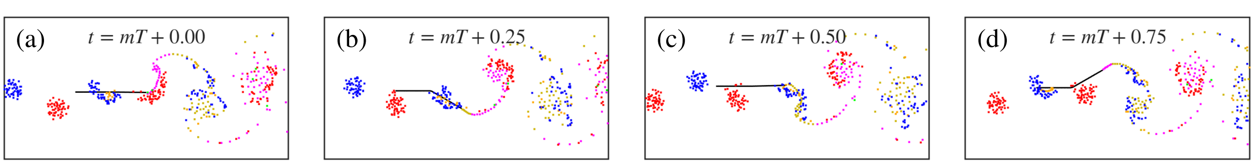

Figure 9. Discrete-vortex plots from the model predictions at four time instants in a cycle of lift oscillation in Figure 8.

In Figure 10, the low-order model evaluates the effect of varying the flap deflection frequency (f_{Flap}) relative to the VG shedding frequency (f_{Shed}). The flap amplitude is fixed at $\delta_{max} = 30°$, and the frequency ratio is swept from 0.25 to 1.0. Altering the deflection frequency changes the period of a cycle of lift oscillation, resulting in $T = 1.45$ s, 2.5 s, 1.65 s, and 1.25 s for $f_{Flap}/f_{Shed} = 0.25, 0.50, 0.75,$ and 1.0, respectively.

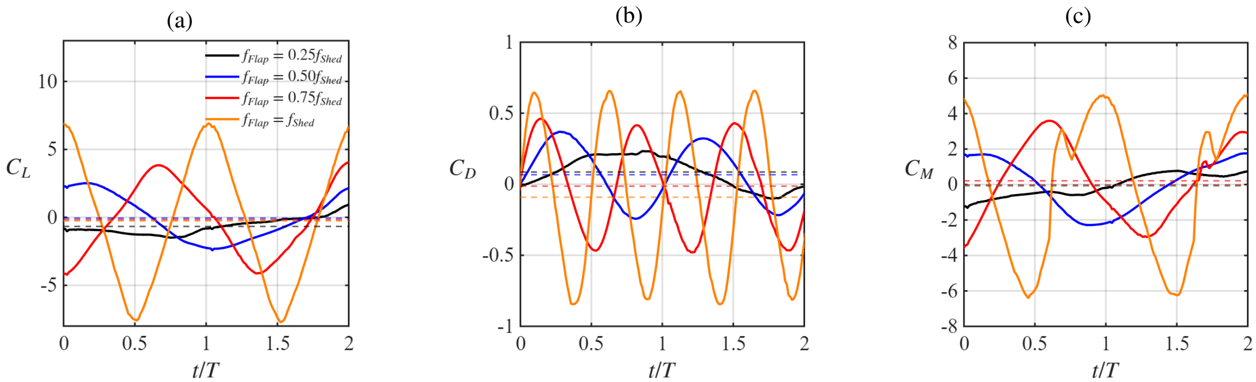

Figure 10. Comparing the effect of varying flap deflection frequency with main-element at 0° incidence in the presence of vortical gusts: (a) C_L, (b) C_D, and (c) C_M predicted by the morphing low-order model.

Quantitatively, the mean aerodynamic loads are highly sensitive to the rate of flap deflection. The mean lift remains negative and progressively degrades as frequency increases: $\bar{C}_L = -0.0358$ ($0.25 f_{Shed}$), -0.1741 ($0.50 f_{Shed}$), -0.2492 ($0.75 f_{Shed}$), and -0.4006 ($1.0 f_{Shed}$). However, increasing the flap frequency yields a distinct thrust generation benefit. The mean drag transitions from a net drag state at lower frequencies ($\bar{C}_D = 0.0926$ at $0.25 f_{Shed}$; 0.0633 at $0.50 f_{Shed}$) to a net thrust-producing state at higher frequencies: $\bar{C}_D = -0.0084$ at $0.75 f_{Shed}$ and -0.0900 at $1.0 f_{Shed}$. The mean pitching moment fluctuates without a defining trend, yielding $\bar{C}_M = -0.0696, -0.1080, -0.1273$, and -0.1020 across the respective frequencies. Beyond the mean values, changing the deflection frequency causes significant phase shifts in the aerodynamic peaks and valleys relative to the vortex positions, despite maintaining the same flap amplitude.

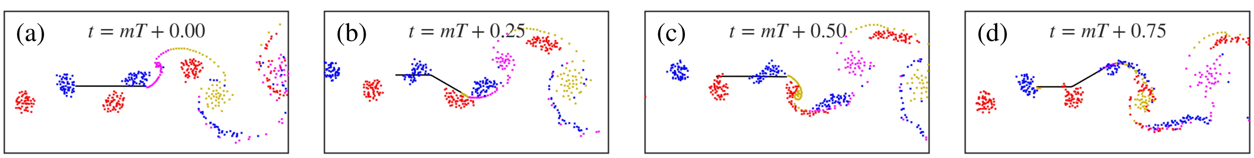

Figure 11. Discrete-vortex predictions at four instants during a lift oscillation cycle for the $0.75 f_{Shed}$ case.

The $0.75 f_{Shed}$ case (Figure 11) demonstrates a phase shift for the lift coefficient: the C_L peak now corresponds to a CW vortex near the LE and a CCW vortex near the hinge, whereas the C_L valley sees the CW vortex near the hinge and the CCW vortex near the LE. The C_D and C_M extrema retain a similar vortex alignment to the $1.0 f_{Shed}$ case (peaks with CW at hinge/CCW at LE; valleys with CW at LE/CCW at hinge). Crucially, for this $0.75 f_{Shed}$ case, the aerodynamic peaks and valleys align directly with the instances when the flap is undergoing its fastest deflection rate, specifically when the flap passes inline with the main element, as shown in Figures 11(a) and 11(c).

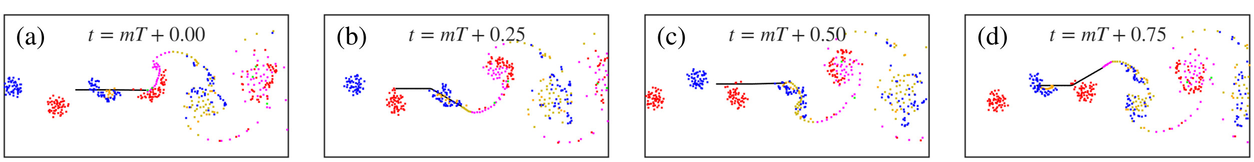

Figure 12. Discrete-vortex predictions at four instants during a lift oscillation cycle from Figure 10 for the $1.0 f_{Shed}$ case.

Whereas, for the $1.0 f_{Shed}$ case (Figure 12), a local peak in C_L, C_D, and C_M consistently occurs when a clockwise (CW) vortex is located near the hinge/mid-chord and a counter-clockwise (CCW) vortex is near the leading edge (LE). Conversely, the aerodynamic valleys for all three coefficients occur when a CW vortex is near the LE and a CCW vortex is near the hinge.

Taken together, these parametric studies provide critical physical intuition for the development of active gust alleviation strategies. The results demonstrate that whereas static flap deflections worsen cyclic aerodynamic loads, dynamic wing-morphing offers sufficient aerodynamic impact to directly counteract vortical gusts. By continuously tuning the amplitude, rate, and phase of the trailing-edge deflection relative to the oncoming gust signature, the induced and shed vorticity can be strategically managed to cancel out adverse load excursions. Ultimately, this indicates that active trailing-edge flaps can be leveraged not merely for passive fatigue mitigation, but as an active mechanism to stabilize flight and opportunistically extract thrust from highly vortical flows.

V. Conclusion

This work presented a novel low order framework for predicting the unsteady aerodynamic loads on morphing airfoils in the presence of vortical gusts (VGs). By integrating unsteady thin-airfoil theory with a discrete vortex representation of leading-edge shedding and vortical gusts, the model provides a computationally efficient alternative to high-fidelity simulations. The primary strength of this framework lies in its rapid parametric sweeps, offering a high-throughput means to evaluate load sensitivities to varying gust characteristics and morphing kinematics.

Validation confirmed the model's accuracy in capturing frequency-dependent lift degradation and transient loading during high-rate flap deflections. The framework excels at predicting impulsive flap motions, which are critical for real-time gust alleviation. However, while the model excellently captures macroscopic loads and large-scale unsteady features (e.g., dynamic stall and leading-edge vortex shedding), it inherently cannot resolve the fully detailed viscous flowfield provided by Navier-Stokes simulations. Additionally, relying on discrete trailing-edge vortex blobs rather than a continuous wake distribution introduces a known vortex sheet discontinuity. This limitation likely contributes to the slight load offsets observed trailing off in slower convective regimes.

Despite these simplifications, the results prove that active trailing-edge flaps possess sufficient aerodynamic impact to counteract VG-induced oscillations. This demonstrates the model's utility in determining how lifting surfaces with trailing edge flaps may be modulated to manage loads in the presence of vortical gusts. Future work will explore implementing a continuous trailing-edge wake to mitigate discrete shedding errors, alongside developing an inverse framework to determine optimal, real-time flap actuation strategies tailored to maintain desired aerodynamic profiles during complex gust encounters.

Acknowledgments

This research was supported by the Coastal Studies Institute through the North Carolina Renewable Ocean Energy Program (NCROEP).

References

[1] Tran, T. T., Craig, J., and Ross, H., "A Study of Wake Characteristics of Marine Turbine Arrays: Preprint," *Renewable Energy*, 2023.

[2] Perez-Becker, S., Marten, D., and Paschereit, C. O., "Active flap control with the trailing edge flap hinge moment as a sensor: using it to estimate local blade inflow conditions and to reduce extreme blade loads and deflections," *Wind Energy Science*, Vol. 6, No. 3, 2021, pp. 791–814. https://doi.org/10.5194/wes-6-791-2021.

[3] Turhan, B., Wang, Z., and Gursul, I., "Interaction of vortex streets with a downstream wing," *Physical Review Fluids*, Vol. 7, No. 9, 2022, p. 094701.

[4] SureshBabu, A., Medina, A., Rockwood, M., Bryant, M., and Gopalarathnam, A., "Theoretical and experimental investigation of an unsteady airfoil in the presence of external flow disturbances," *Journal of Fluid Mechanics*, Vol. 921, 2021, p. A21. https://doi.org/10.1017/jfm.2021.484.

[5] Rival, D., Prangemeier, T., and Tropea, C., "The Influence of Airfoil Kinematics on the Formation of Leading-Edge Vortices in Bio-Inspired Flight," *Experiments in Fluids*, Vol. 46, No. 5, 2009, pp. 823–833. https://doi.org/10.1007/s00348-008-0586-1.

[6] Ramesh, K., Gopalarathnam, A., Granlund, K., Ol, M. V., and Edwards, J. R., "Discrete-vortex method with novel shedding criterion for unsteady aerofoil flows with intermittent leading-edge vortex shedding," *Journal of Fluid Mechanics*, Vol. 751, 2014, pp. 500–538. https://doi.org/10.1017/jfm.2014.297.

[7] Martínez-Carmena, A., and Ramesh, K., "Inviscid modeling of unsteady morphing airfoils using a discrete-vortex method," *Theoretical and Computational Fluid Dynamics*, Vol. 38, No. 6, 2024, pp. 845–862. https://doi.org/10.1007/s00162-023-00678-7.

[8] Medina, A., Ol, M. V., Mancini, P., and Jones, A., "Revisiting Conventional Flaps at High Deflection Rate," *AIAA Journal*, Vol. 55, No. 8, 2017, pp. 2676–2685. https://doi.org/10.2514/1.J055754.